

## 2.5D forward and inverse modeling for interpreting low-frequency electromagnetic measurements

A. Abubakar<sup>1</sup>, T. M. Habashy<sup>1</sup>, V. L. Druskin<sup>1</sup>, L. Knizhnerman<sup>2</sup>, and D. Alumbaugh<sup>3</sup>

### ABSTRACT

We present 2.5D fast and rigorous forward and inversion algorithms for deep electromagnetic (EM) applications that include crosswell and controlled-source EM measurements. The forward algorithm is based on a finite-difference approach in which a multifrontal LU decomposition algorithm simulates multisource experiments at nearly the cost of simulating one single-source experiment for each frequency of operation. When the size of the linear system of equations is large, the use of this noniterative solver is impractical. Hence, we use the optimal grid technique to limit the number of unknowns in the forward problem. The inversion algorithm employs a regularized Gauss-Newton minimization approach with a multiplicative cost function. By using this multiplicative cost function, we do not need a priori data to determine the so-called regularization parameter in the optimization process, making the algorithm fully automated. The algorithm is equipped with two regularization cost functions that allow us to reconstruct either a smooth or a sharp conductivity image. To increase the robustness of the algorithm, we also constrain the minimization and use a line-search approach to guarantee the reduction of the cost function after each iteration. To demonstrate the pros and cons of the algorithm, we present synthetic and field data inversion results for crosswell and controlled-source EM measurements.

### INTRODUCTION

Electromagnetic (EM) methods are important tools for appraising a reservoir because of their sensitivity to conductivity, which is a function of fluid saturation. One of the well-known EM techniques is the single-well induction logging measurement, used as a wireline

measurement and as a measurement while drilling to estimate near-wellbore conductivity. This induction logging measurement has a sensitivity of up to a few meters from the well and is a function of the separation between the transmitter and the receiver, the frequency of operation, and the resistivity distribution.

To reach deeper into the reservoir, a crosswell EM technology has been developed (Spies and Habashy, 1995; Wilt et al., 1995). The system operates similarly to the single-well logging tool except with transmitters and receivers deployed in separate wells and at a lower frequency of operation. During a crosswell survey, the receiver array initially is lowered into one well to the bottom of the survey-depth interval. Then the transmitter is lowered into a second well and is moved to log the entire survey-depth interval. During logging, the transmitter broadcasts EM signals at prescribed frequencies recorded at the receiver well. After the transmitter run is completed, the receiver array is moved to the next depth station in the survey interval, and the process is repeated until the entire depth interval is covered.

When the data set has been collected, an inversion process converts the EM signals to a conductivity distribution map of the region between the wells. Because the survey involves only two wells, one can usually assume a 2D geometry in the inversion, i.e., the conductivity distribution is invariant along the direction perpendicular to the plane that contains the wells. Processing data that are collected only using two wells with a 3D approach might not produce a reasonable geologic image because of the nonuniqueness of the problem.

Another type of EM measurement that can reach deep into the reservoir is the marine controlled-source electromagnetic method (CSEM). The depth of investigation of a CSEM measurement is even larger than a crosswell measurement. This method has received increased attention as a hydrocarbon exploration tool (e.g., MacGregor and Sinha, 2000; Eidesmo et al., 2002; Johansen et al., 2005). The interest has resulted from the technique's ability to directly detect the presence of thin, hydrocarbon-bearing layers.

<sup>1</sup>Manuscript received by the Editor 20 August 2007; revised manuscript received 18 January 2008; published online 1 July 2008.

<sup>2</sup>Schlumberger-Doll Research, Cambridge, Massachusetts, U.S.A. E-mail: abubakar@slb.com; habashy1@slb.com; druskin1@boston.oilfield.slb.com.

<sup>3</sup>Center of Geophysical Expedition, Moscow, Russia. E-mail: mmd@cge.ru.

<sup>3</sup>Schlumberger-EMI, Richmond, California, U.S.A. E-mail: dalumbaugh@slb.com.

© 2008 Society of Exploration Geophysicists. All rights reserved.

Initially, the data are analyzed by plotting the amplitude of the electric field versus source-receiver offset and then by normalizing the amplitude of the electric field acquired over a possible hydrocarbon prospect by the amplitude of the electric field measured over a similar nonhydrocarbon-bearing area (Eidesmo et al., 2002). Because the presence of hydrocarbon increases the amplitude of the measured electric field, the normalized value will be greater than unity for areas containing resistive anomalies and unity or less for nonhydrocarbon-bearing zones.

Although this method provides information on the presence of hydrocarbon and some information on the horizontal location and extent of the reservoir, it is difficult to discern a reservoir's depth or true geometry. To provide this additional information, one must use a full nonlinear inversion approach. For approximate images of the subsurface conductivity structure, fast imaging techniques such as migration wavefield imaging, e.g., Tompkins (2004) and Mittet et al. (2005), are helpful. These approaches generally provide low-resolution images that can be difficult to interpret in terms of true conductivity structures.

For both crosswell EM and CSEM measurements, full nonlinear inversion algorithms such as those used by Newman and Alumbaugh (1997), Abubakar and van den Berg (2000), Newman and Boggs (2004), and Gribenko and Zhdanov (2007) might tend to be expensive computationally, resulting from the forward-modeling schemes that rely on iterative matrix solution techniques. These methods generally require that each source excitation be solved one at a time. Consequently, a 2.5D inversion can take hours to days on a standard serial computer, whereas the 3D inversion can be tractable only using massively parallel resources.

In this paper, we present efficient 2.5D forward and inversion algorithms. Unlike any other 2.5D forward algorithms (Allers et al., 1994; Druskin and Knizhnerman, 1994; Torres-Verdín and Habashy, 1994; Abubakar et al., 2006), we use a multifrontal LU decomposition (Davis and Duff, 1997) to invert the stiffness matrix. By using this direct matrix inversion technique, we can simulate multisource experiments at nearly the cost of simulating only one single-source experiment. This feature is very important because in the inversion we need to use data from more than one source position/orientation. The direct matrix inversion technique is accomplished using the optimal grid technique (Ingerman et al., 2000) to extend the boundaries of the computational domain to infinity and a diagonal anisotropic material averaging formula (Keller, 1964) to assign appropriate conductivity values on the finite-difference grid nodes.

For the inversion algorithm, we use a regularized Gauss-Newton minimization approach as described in Habashy and Abubakar (2004) with a multiplicative cost function (van den Berg et al., 1999). By using this multiplicative cost function, we do not need to determine the so-called regularization parameter in the optimization process, making the algorithm fully automated. The algorithm is equipped with two regularization functions to produce either a smooth or a sharp conductivity distribution (van den Berg and Abubakar, 2001).

To illustrate the capabilities of our methods, we apply the inversion scheme to synthetic and field data sets. For the crosswell EM measurement, we use data collected in Lost Hill, California, U.S.A. (Wilt et al., 2005). For the CSEM measurement, we use data collected in Troll field, Norway (Hoversten et al., 2005 and Johansen et al., 2005).

## THE FORWARD ALGORITHM

We formulate the problem in the frequency domain with the time convention  $\exp(-i\omega t)$ , where  $i^2 = -1$ ,  $\omega$  is the angular frequency, and  $t$  is the time variable:

$$\nabla \times \mathbf{E} - i\omega\mu\mathbf{H} = \mathbf{K}, \quad (1)$$

$$\nabla \times \mathbf{H} - (\boldsymbol{\sigma} - i\omega\boldsymbol{\epsilon}) \cdot \mathbf{E} = \mathbf{J}. \quad (2)$$

The zero boundary condition is at infinity. Here,  $\mathbf{E}(x,y,z)$  and  $\mathbf{H}(x,y,z)$  are the electric and magnetic field vectors, respectively, and  $\mathbf{J}(x,y,z)$  and  $\mathbf{K}(x,y,z)$  are the electric and magnetic current sources, respectively. The conductivity  $\boldsymbol{\sigma}(x,z)$  and the permittivity  $\boldsymbol{\epsilon}(x,z)$  are diagonal tensors invariant along the  $y$ -axis, and the magnetic permeability  $\mu$  is a scalar constant. In equations 1 and 2,  $\nabla = (\partial_x, \partial_y, \partial_z)$  is the spatial differentiation operator. Eliminating  $\mathbf{H}$  from equations 1 and 2, we obtain

$$\nabla \times \nabla \times \mathbf{E} - (i\omega\mu\boldsymbol{\sigma} + \omega^2\mu\boldsymbol{\epsilon}) \cdot \mathbf{E} = \nabla \times \mathbf{K} + i\omega\mu\mathbf{J}. \quad (3)$$

Although we have an unbounded problem with the EM field vanishing at infinity, for computational purposes we assume we have a bounded domain of interest, or  $D = \{(x,y,z) : x_{\min} < x < x_{\max}, y_{\min} < y < y_{\max}, z_{\min} < z < z_{\max}\}$ . On the outer boundaries, we impose the following condition on the tangential component of the electrical field:

$$\mathbf{E} \times \mathbf{n} = \mathbf{0}, \quad (4)$$

where  $\mathbf{n}$  is a unit normal vector. Unlike the case of wave-propagation problems, a truncation of the infinite domain does not cause resonances or large reflections because of the exponential decay of the EM field in lossy media in the diffusive regime. To model the point source we use the discrete pseudo-delta-function approach, which is a rather standard approach in finite-difference modeling. The results are accurate some distance from the singularity point (the transmitter location).

Equations 3 and 4 are discretized according to the finite-difference method on the staggered 3D Yee grid (Yee, 1966). To take advantage of the 2D structure of the configuration, we introduce the 1D spatial Fourier transform and its inverse with respect to the  $y$ -coordinate axis:

$$\tilde{u} = \mathcal{F}\{u\} = \int_{y=-\infty}^{\infty} dy \exp(ik_y y) u(x, y, z), \quad (5)$$

$$u = \mathcal{F}^{-1}\{\tilde{u}\} = \frac{1}{2\pi} \int_{k_y=-\infty}^{\infty} dk_y \exp(-ik_y y) \tilde{u}(x, k_y, z). \quad (6)$$

We apply this Fourier transform to equation 3 to obtain

$$\tilde{\nabla} \times \tilde{\nabla} \times \tilde{\mathbf{E}} - (i\omega\mu\boldsymbol{\sigma} + \omega^2\mu\boldsymbol{\epsilon}) \cdot \tilde{\mathbf{E}} = \nabla \times \tilde{\mathbf{K}} + i\omega\mu\tilde{\mathbf{J}}, \quad (7)$$

where  $\tilde{\nabla} = (\partial_x, k_y, \partial_z)$ .

To solve this system of equations quickly, the inner computational domain is discretized using a uniform Cartesian grid. The boundaries are then extended away from this uniform region in the  $x$ - and

$z$ -directions with as few cells as possible, using the optimal grid technique described by Ingberman et al. (2000). A typical finite-difference grid that is used in the crosswell configuration is shown in Figure 1.

In Figure 1, the domain of investigation ( $x = -28.5$  to  $97.5$  m;  $z = 183.75$  to  $324.75$  m) is discretized using  $44 \times 96$  uniform grids. We need only 11 optimal grid nodes in each direction (10 nonuniform grids) to extend the computational domain to infinity. As an illustration, the nodes in the  $x$ -direction that extend the computational domain to  $+\infty$  are  $100.5, 105.12, 117.53, 142.93, 193.72, 296.88, 508.87, 947.55, 1866.5, 3891.1$ , and  $10,101$  m; the ones that extend the computational domain to  $-\infty$  are  $-10,032, -3822.1, -1797.5, -878.55, -439.87, -227.88, -124.72, -73.931, -48.534, -36.124$ , and  $-31.5$  m. The extensions in the  $z$ -direction are found in a similar way. In total, we have 65 nodes in  $x$ -direction and 117 nodes in the  $z$ -direction.

Upon discretization, we obtain the finite-difference counterpart of equation 3, written in matrix notation as

$$\tilde{\mathcal{A}} \cdot \tilde{\mathbf{x}} = \tilde{\mathbf{b}}, \quad (8)$$

where  $\tilde{\mathcal{A}}$  is a stiffness matrix resulting from the left side of equation 7,  $\tilde{\mathbf{x}}$  is a vector containing the electric field at all nodes, and  $\tilde{\mathbf{b}}$  is a vector resulting from the right side of equation 7 at all nodes.

The model might not conform to the nonuniform Cartesian grids. To use these grids (calculated using the optimal grid technique) without sacrificing accuracy, a material-averaging formula based on Keller (1964) is used. It upscales from the model parameter, which can be very finely discretized, to the finite-difference grid, which is as coarse as possible, while maintaining an accurate solution. Note that the material-averaging formula given in Keller (1964) is valid only for the diagonal anisotropic medium. For a full anisotropic medium, material averaging as described in Moskow et al. (1999) or in Habashy and Abubakar (2007) can be used.

The resulting linear system of equations (the stiffness matrix) in equation 8 is then solved using a multifrontal LU decomposition method developed by Davis and Duff (1997) that solves for all source excitations simultaneously. This feature provides a rapid solution for the inverse problem, in which the solution for many source locations and orientations can be achieved by inverting the stiffness matrix only once. For a problem with  $N$  total nodes, the optimal multifrontal LU method takes  $O(N^{1.5})$  operations for matrix factorization and  $O(N \log N)$  operations for any additional source calculation (Davis, 2007).

This method also provides very accurate solutions by avoiding slow or nonconverging problems associated with iterative matrix inversion techniques. Hence, the solver has no difficulty simulating very-low-frequency problems such as in the CSEM problem or very-high-contrast configurations such as in the crosswell EM problem. However, because the frequency information is contained in the stiffness matrix, each new frequency requires an additional stiffness matrix inversion. Thus, the total run time is dependent on the number of cells in the model times the number of frequencies to be simulated.

After solving equation 8, the electric and the magnetic field vectors at the finite-difference nodes can be obtained from

$$\mathbf{E}(x, y, z) = \frac{1}{2\pi} \int_{k_y=-\infty}^{\infty} dk_y \exp(-ik_y y) \tilde{\mathbf{E}}(x, k_y, z) \quad (9)$$

and

$$\mathbf{H}(x, y, z) = \frac{1}{i\omega\mu} \nabla \times \mathbf{E}(x, y, z). \quad (10)$$

Use of the staggered Yee grid requires that the fields be located at a priori defined locations, which might not necessarily correspond to the true source and receiver positions. To obtain fields at true receiver positions that are caused by sources at true locations, we interpolate from the true source point to the staggered Yee grid-field locations to provide for the source vector. For the receivers, we reverse this process, i.e., interpolate from the staggered Yee grid to the receiver location.

For the CSEM problem, we deal with this issue differently. Because the receivers are located on the seafloor, some components of the electric and magnetic vectors are discontinuous. Therefore, in this case, we extrapolate to obtain the fields at the receiver positions from nodes above the seafloor.

## THE INVERSION ALGORITHM

We consider a discrete nonlinear inverse problem described by the following operator equation:

$$\mathbf{d}^{\text{obs}} = \mathbf{s}(\mathbf{m}), \quad (11)$$

where

$$\begin{aligned} \mathbf{d}^{\text{obs}} &= [d^{\text{obs}}(\mathbf{r}_i^S, \mathbf{r}_j^R, \omega_k), \\ &i = 1, 2, \dots, I; j = 1, 2, \dots, J; k = 1, 2, \dots, K]^T \end{aligned}$$

is the vector of measured data where  $\mathbf{r}_i^S$ ,  $\mathbf{r}_j^R$ , and  $\omega_k$  are the source position vector, the receiver position vector, and the frequency of operation, respectively. The superscript  $T$  denotes the transpose of a vector. We use a lexicographical ordering of the unknowns to map the 3D array indices to 1D column indices  $(i, j, k) \rightarrow K \times J \times (i-1) + K \times (j-1) + k$ . The symbol  $\mathbf{s}$  is the vector of data computed using the forward algorithm as described in the previous section for the vector model parameters:

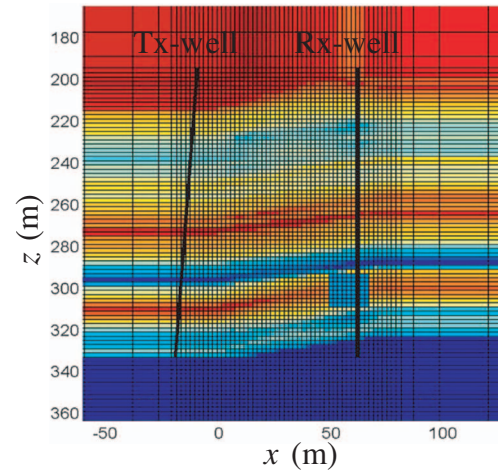


Figure 1. A typical finite-difference grid used in the crosswell configuration. The domain of interest in which transmitters, receivers, and anomalies are located are discretized using a uniform Cartesian grid. The boundaries are extended to infinity using the optimal grid technique.

$$\mathbf{m} = [m(x_l, z_q), l = 1, 2, \dots, L; q = 1, 2, \dots, Q], \quad (12)$$

where  $x_l$  and  $z_q$  denote the center of the 2D discretization cell. We again use a lexicographical ordering of the unknowns to map the 2D array indices to 1D column indices  $(l, q) \rightarrow Q \times (l - 1) + q$ . We assume there are  $I \times J \times K$  number of data points in the experiment and that the configuration can be described by  $L \times Q$  model parameters.

In the crosswell EM problem, the data are the component of the magnetic field, which is parallel to the borehole axis. In the CSEM problem, the data can be any component of the magnetic or electric field. The unknown model parameter  $m(x_l, z_q) = \sigma(x_l, z_q)/\sigma_0$  is the normalized conductivity, where  $\sigma_0$  is a constant conductivity. In our implementation,  $\sigma_0$  is chosen to be a spatial average of the initial model used in the inversion process.

We pose the inverse problem as a minimization problem with a multiplicative cost function (van den Berg et al., 1999; van den Berg and Abubakar, 2001; Habashy and Abubakar, 2004). Hence, at the  $n$ th iteration we reconstruct  $\mathbf{m}_n$  that minimizes

$$\Phi_n(\mathbf{m}) = \phi^d(\mathbf{m}) \times \phi_n^m(\mathbf{m}), \quad (13)$$

where  $\phi^d$  is a measure of the data misfit

$$\phi^d(\mathbf{m}) = \frac{1}{2} \sum_{k=1}^K \eta_k \frac{\sum_{i=1}^I \sum_{j=1}^J |W_{d;i,j,k}[d_{i,j,k}^{\text{obs}} - S_{i,j,k}(\mathbf{m})]|^2}{\sum_{i=1}^I \sum_{j=1}^J |W_{d;i,j,k} d_{i,j,k}^{\text{obs}}|^2}, \quad (14)$$

in which  $|\cdot|$  denotes the absolute value and  $\mathcal{W}_d$  is the data weighting matrix whose elements are estimates of the standard deviations of the noise. The symbol  $\eta_k$  is the frequency weighting:

$$\eta_k = \frac{\omega_k^{-2}}{\sum_{s=1}^K \omega_s^{-2}}, \quad (15)$$

where  $\omega$  is the angular frequency. This particular choice of the frequency weighting puts each frequency data component on an equal footing in the optimization process.

The nonzero regularization function  $\phi_n^m$  is a measure of the variation of the model parameters and is given by

$$\begin{aligned} \phi_n^m(\mathbf{m}) &= \int_D [b_n^2(x, z) \{|\nabla_t[m(x, z) - m^{\text{ref}}(x, z)]|^2 + \delta_n^2\}] dx dz, \end{aligned} \quad (16)$$

where  $\nabla_t = [\partial_x \partial_z]^T$  denotes spatial differentiation and the weight  $b_n(x, z)$  is given by

$$b_n^2(x, z) = \frac{1}{\int_D \{|\nabla_t[m_n(x, z) - m^{\text{ref}}(x, z)]|^2 + \delta_n^2\} dx dz} \quad (17)$$

for the  $L_2$ -norm regularizer and

$$b_n^2(x, z) = \frac{1}{V |\nabla_t[m_n(x, z) - m^{\text{ref}}(x, z)]|^2 + \delta_n^2} \quad (18)$$

for the weighted  $L_2$ -norm regularizer (van den Berg and Abubakar, 2001). The  $L_2$ -norm regularizer is known to favor a smooth profile, whereas the weighted  $L_2$ -norm regularizer is known for its ability to preserve edges. The symbol  $V = \int_D dx dz$  denotes the area of the computational domain, and  $\mathbf{m}^{\text{ref}}$  is the known reference model.

In our implementation when there is no a priori information available, we choose the initial model as the known reference model. For the  $L_2$ -norm regularizer, the weight  $b_n(x, z)$  is independent of the spatial position. The  $\delta_n^2$  is a constant, chosen to be equal to

$$\delta_n^2 = \frac{\phi^d(\mathbf{m}_n)}{\Delta x \Delta z}, \quad (19)$$

where  $\Delta x$  and  $\Delta z$  are the widths of the discretization cell in the  $x$ - and  $z$ -directions.

Note that the presence of  $\delta_n^2$  ensures the regularization factor will be nonzero. This weighted  $L_2$ -norm regularization factor belongs to the same class as the well-known total variation regularization (Charbonnier et al., 1996; Dobson and Santosa, 1996; Vogel and Oman, 1996; Farquharson and Oldenburg, 1998) and the focusing regularization function (Portniaguine and Zhdanov, 1999). Although this weighted  $L_2$ -norm regularization cost function has all the advantages of the total variation regularization function, it is still quadratic. This means it has a well-defined gradient and is more suitable for a Gauss-Newton approach.

To solve equation 13, we use a Gauss-Newton minimization approach. At the  $n$ th iteration, we obtain a set of linear equations for the search vector  $\mathbf{p}_n$  that identifies the minimum of the approximated quadratic cost function:

$$\mathcal{H}_n \cdot \mathbf{p}_n = -\mathbf{g}_n, \quad (20)$$

where the Hessian matrix is given by

$$\begin{aligned} \mathcal{H}_n &= \phi_n^m(\mathbf{m}_n) (\mathcal{J}_n^T \cdot \mathcal{W}_d^T \cdot \mathcal{W}_d \cdot \mathcal{J}_n^T + \mathcal{Q}_n) + \phi^d(\mathbf{m}_n) \mathcal{L}(\mathbf{m}_n) \\ &\quad + [\mathcal{L}(\mathbf{m}_n) \cdot \mathbf{m}_n] \{ \mathcal{J}_n^T \cdot \mathcal{W}_d^T \cdot \mathcal{W}_d \cdot [\mathbf{d}^{\text{obs}} - \mathbf{s}(\mathbf{m}_n)] \} \\ &\quad + [\mathcal{J}_n^T \cdot \mathcal{W}_d^T \cdot \mathcal{W}_d \cdot [\mathbf{d}^{\text{obs}} - \mathbf{s}(\mathbf{m}_n)]] [\mathcal{L}(\mathbf{m}_n) \cdot \mathbf{m}_n]. \end{aligned} \quad (21)$$

To make the Hessian matrix nonnegative definite, in equation 21 we neglect the second-order derivative of the cost function, the matrix term  $\mathcal{Q}_n$ , and the nonsymmetric terms (the third and fourth terms). Also, by using the fact that  $\phi_n^m(\mathbf{m}_n) = 1$ , the Hessian matrix becomes

$$\mathcal{H}_n \approx \mathcal{J}_n^T \cdot \mathcal{W}_d^T \cdot \mathcal{W}_d \cdot \mathcal{J}_n^T + \phi^d(\mathbf{m}_n) \mathcal{L}(\mathbf{m}_n). \quad (22)$$

The matrices  $\mathcal{J}_n$  and  $\mathcal{L}(\mathbf{m}_n)$  are defined in the following paragraphs.

The gradient of the cost function is given by

$$\begin{aligned} \mathbf{g}_n &= -\phi_n^m(\mathbf{m}_n) \{ \mathcal{J}_n^T \cdot \mathcal{W}_d^T \cdot \mathcal{W}_d \cdot [\mathbf{d}^{\text{obs}} - \mathbf{s}(\mathbf{m}_n)] \} \\ &\quad + \phi^d(\mathbf{m}_n) \mathcal{L}(\mathbf{m}_n) \cdot \mathbf{m}_n \\ &= -\mathcal{J}_n^T \cdot \mathcal{W}_d^T \cdot \mathcal{W}_d [\mathbf{d}^{\text{obs}} - \mathbf{s}(\mathbf{m}_n)] \\ &\quad + \phi^d(\mathbf{m}_n) \mathcal{L}(\mathbf{m}_n) \cdot \mathbf{m}_n, \end{aligned} \quad (23)$$

where the derivative of the regularization cost function  $\phi_n^m$  with respect to  $\mathbf{m}$  is given by

$$\mathcal{L}(\mathbf{m}_n) \cdot \mathbf{m}_n = \nabla_t \cdot [b_n^2(x,z) \nabla_t m_n(x,z)]. \quad (24)$$

Hence, this multiplicative cost function given in equation 13 is equivalent to the following standard cost function:

$$\Phi_n(\mathbf{m}) = \phi^d(\mathbf{m}) + \lambda_n \phi_n^m(\mathbf{m}), \quad (25)$$

with the choice of the regularization parameter  $\lambda_n$  to be equal to

$$\lambda_n = \frac{\phi^d(\mathbf{m}_n)}{\phi_n^m(\mathbf{m}_n)} = \phi^d(\mathbf{m}_n), \quad (26)$$

because  $\phi_n^m(\mathbf{m}_n)$  is equal to unity. This multiplicative cost function is equivalent to the standard cost function given above because the normal equations within the Gauss-Newton approximation are exactly the same.

This procedure minimizes the regularization factor with a large weight at the beginning of the optimization process because the value of  $\phi^d(\mathbf{m})$  is still large. In this case, the search direction is predominantly steepest descent, which is a more appropriate approach to use in the initial steps of the iteration process because it tends to suppress large swings in the search direction. As the iteration proceeds, the optimization process gradually minimizes the error in the data misfit when the regularization factor  $\phi_n^m(\mathbf{m})$  remains a nearly constant value close to unity. In this case, the search direction corresponds to the Newton search method, which is a more appropriate approach to use as we near the minimum of the data misfit cost function  $\phi^d(\mathbf{m})$ , where the quadratic model of the cost function becomes more accurate.

If noise is present in the data,  $\phi^d(\mathbf{m})$  will remain at a certain value during the optimization process. Hence, the weight on the regularization factor will be more significant. In this way, the noise will be suppressed at all times in the inversion process; in addition, the need for a larger regularization when the data contain noise will be fulfilled automatically, as suggested by Rudin et al. (1992) and Chan and Wong (1998).

In equations 22 and 23,  $\mathcal{J}_n = \mathcal{J}(\mathbf{m}_n)$  is the  $(I \times J \times K) \times (L \times Q)$  Jacobian matrix, given by

$$\begin{aligned} \mathcal{J}_{i,j,k;l,q;n} &= \left. \frac{\eta_k}{\sum_{s=1}^I \sum_{r=1}^J |W_{d;s,r,k} d_{s,r,k}^{\text{obs}}|^2} \frac{\partial S_{i,j,k}(\mathbf{m})}{\partial m_{l,q}} \right|_{\mathbf{m}=\mathbf{m}_n} \\ &= \left. \frac{\eta_k \sigma_0}{\sum_{s=1}^I \sum_{r=1}^J |W_{d;s,r,k} d_{s,r,k}^{\text{obs}}|^2} \frac{\partial S_{i,j,k}(\mathbf{m})}{\partial \sigma_{l,q}} \right|_{\mathbf{m}=\mathbf{m}_n}, \end{aligned} \quad (27)$$

where the explicit expressions for  $\partial S / \partial \sigma$  for different transmitter and receiver types are given in Appendix A. This Jacobian matrix is calculated using an adjoint formulation (McGillivray and Oldenburg, 1990; Mackie and Madden, 1993; Rodi and Mackie, 2001), which requires a set of forward computations whereby the roles of the transmitters and receivers are interchanged. If an iterative solution is used to solve the forward problem, this requires an extra forward solution at each Gauss-Newton search step for each receiver and/or transmitter. However, because we are using a forward code

with a multifrontal LU decomposition solver (a direct solver), we need only one forward call to calculate the data misfit and to generate the Jacobian matrix because the stiffness matrix has already been inverted. Hence, the extra computational effort to generate this Jacobian matrix is negligible.

The Hessian matrix  $\mathcal{H}_n$  can be large, so we solve the linear system of equations in equation 20 using an iterative method. Multifrontal LU decomposition is inefficient because the Hessian matrix is full. To that end, we first rewrite equation 20 as

$$\mathcal{K} \cdot \mathbf{p}_n = \mathbf{f}, \quad (28)$$

where  $\mathcal{K} = \mathcal{H}_n$  and  $\mathbf{f} = -\mathbf{g}_n$ . Because  $\mathcal{K}$  is a self-adjoint matrix, we use a conjugate gradient least-squares (CGLS) scheme (Golub and van Loan, 1989) to solve this linear system of equations. This CGLS scheme starts with the initial values

$$\mathbf{v}^{(0)} = \mathbf{f} - \mathcal{K} \cdot \mathbf{p}_n^{(0)}, \quad \text{ERR}^{(0)} = \frac{\|\mathbf{v}^{(0)}\|}{\|\mathbf{f}\|}, \quad (29)$$

where  $\mathbf{p}_n^{(0)} = \mathbf{p}_{n-1}$ . Next, we compute successively for  $N = 1, 2, \dots$ ,

$$\mathbf{A}^{(N)} = \langle \mathbf{v}^{(N-1)}, \mathcal{K} \cdot \mathbf{v}^{(N-1)} \rangle,$$

$$\mathbf{u}^{(N)} = \mathbf{v}^{(N-1)}, \quad N = 1,$$

$$= \mathbf{v}^{(N-1)} + \frac{\mathbf{A}^{(N)}}{\mathbf{A}^{(N-1)}} \mathbf{u}^{(N-1)}, \quad N > 1,$$

$$B^{(N)} = \|\mathcal{K} \cdot \mathbf{u}^{(N)}\|^2,$$

$$\mathbf{p}_n^{(N)} = \mathbf{p}_n^{(N-1)} + \frac{\mathbf{A}^{(N)}}{B^{(N)}} \mathbf{u}^{(N)},$$

$$\mathbf{v}^{(N)} = \mathbf{f} - \mathcal{K} \cdot \mathbf{p}_n^{(N)}, \quad \text{ERR}^{(N)} = \frac{\|\mathbf{v}^{(N)}\|}{\|\mathbf{f}\|}, \quad (30)$$

where

$$\|\mathbf{u}\| = \sqrt{\Delta x \Delta z \sum_{p=1}^P \sum_{q=1}^Q |u_{p,q}|} \quad (31)$$

denotes the  $L_2$ -norm of a vector. This CGLS iteration process stops if one of the following conditions occurs:

- The rms of the relative error reaches a prescribed value  $\eta$ ,

$$\text{ERR}^{(N)} \leq \eta, \quad (32)$$

where  $\eta$  is a predetermined a priori value that must be provided by the user.

- The total number of iterations  $N_{\max}$  exceeds a prescribed maximum. In our implementation this  $N_{\max}$  is set equal to the total number of unknowns  $P \times Q$ .

After the search vector  $\mathbf{p}_n = \mathbf{p}_n^{(N)}$  is obtained, the unknown model parameters are updated as follows:

$$\mathbf{m}_{n+1} = \mathbf{m}_n + \nu_n \mathbf{p}_n, \quad (33)$$

where  $\nu_n$  is a scalar constant parameter to be determined by a line-search algorithm. In the implementation, we start with the full step, i.e.,  $\nu_n = 1$ , and check if it reduces the value of the cost function  $\Phi_n$ . If not, we backtrack along the Gauss-Newton step until we have an acceptable step. Because the Gauss-Newton step is a descent direc-

tion for  $\Phi_n$ , we are guaranteed to find an acceptable step. In this procedure,  $\nu_n$  is selected such that

$$\Phi_n(\mathbf{m}_n + \nu_n \mathbf{p}_n) \leq \Phi_n(\mathbf{m}_n) + \alpha \nu_n \delta \Phi_{n+1}, \quad (34)$$

where  $0 < \alpha < 1$  is a fractional number set to be quite small, i.e.,  $\alpha$  to  $10^{-4}$ , so that hardly more than a decrease in the cost function value is required (Dennis and Schnabel, 1983). The parameter  $\delta \Phi_{n+1}$  is the rate of decrease of  $\phi(\mathbf{m})$  at  $\mathbf{m}_n$  along the direction  $\mathbf{p}_n$ , given by

$$\delta \Phi_{n+1} = \left. \frac{\partial}{\partial \nu} \Phi_n(\mathbf{m}_n + \nu \mathbf{p}_n) \right|_{\nu=0} = \mathbf{g}_n^T \cdot \mathbf{p}_n. \quad (35)$$

If, at the  $(n+1)$  iteration,  $\nu_n^{(m)}$  is the current step-length that does not satisfy the condition in equation 34, we compute the next back-tracking step-length  $\nu_n^{(m+1)}$  by searching for the minimum of the cost function, assuming a quadratic approximation in  $\nu$ . Hence,  $\nu_k^{(m+1)}$  for  $m = 0, 1, 2, \dots$  is given by

$$\nu_n^{(m+1)} = \frac{-0.5[\nu_k^{(m)}]^2 \delta \Phi_{n+1}}{\Phi_n(\mathbf{m}_n + \nu_n^{(m)} \mathbf{p}_n) - \Phi_n(\mathbf{m}_n) - \nu_n^{(m)} \delta \Phi_{n+1}}. \quad (36)$$

In general, decreasing  $\nu_n^{(m+1)}$  too much can excessively slow the iterative process. To prevent this, we set  $\nu_n^{(m+1)} = 0.1 \nu_n^{(m)}$  if  $\nu_n^{(m+1)} < 0.1 \nu_n^{(m)}$  (but with  $\nu_n$  not to decrease below 0.1, i.e.,  $\nu_{\min} = 0.1$ , to guard against a value of  $\nu$  that is too small) and then proceed with the Gauss-Newton step.

To impose a priori information of maximum and minimum bounds on the unknown parameters, we constrain them using a nonlinear transformation of the form

$$m = \frac{m^{\max} \exp(c) + m^{\min} \exp(-c)}{\exp(c) + \exp(-c)}, \quad (37)$$

$$-\infty < c < +\infty,$$

where  $m^{\max}$  and  $m^{\min}$  are the upper and lower bounds on the physical model parameter  $m$ . For simplicity, we neglect the subscripts  $l$  and  $q$ . It is clear that  $m \rightarrow m^{\min}$  as  $c \rightarrow -\infty$  and  $m \rightarrow m^{\max}$  as  $c \rightarrow +\infty$ . This nonlinear transformation forces the reconstruction of the model parameters to lie always within their prescribed bounds.

By using this nonlinear transformation in a standard way, we should update the auxiliary unknown parameters  $c$  instead of the model parameters  $m$ . However, by using the relation

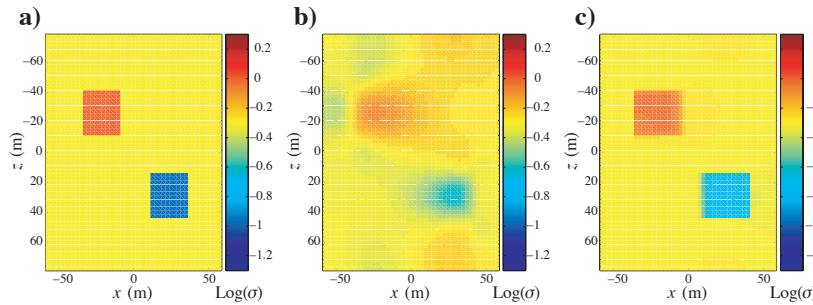


Figure 2. The (a) true and (b) inverted conductivity using the  $L_2$ -norm regularization factor and (c) the weighted  $L_2$ -norm regularization factor.

$$p = \frac{dm}{dc} q = 2 \frac{(m^{\max} - m)(m - m^{\min})}{m^{\max} - m^{\min}} q, \quad (38)$$

where  $p$  is the Gauss-Newton search step with respect to  $m$  and  $q$  is the Gauss-Newton search step with respect to  $c$ , we obtain the following explicit relationships between the two successive iterates  $m_{n+1}$  and  $m_n$  of  $m$ :

$$m_{n+1} = \frac{m^{\max}(m_n - m^{\min}) \exp(\alpha_n \nu_n p_n) + m^{\min}(m^{\max} - m_n)}{(m_n - m^{\min}) \exp(\alpha_n \nu_n p_n) + (m^{\max} - m_n)} q \quad \text{for } p_n < 0 \quad (39)$$

and

$$m_{n+1} = \frac{m^{\max}(m_n - m^{\min}) + m^{\min}(m^{\max} - m_n) \exp(-\alpha_n \nu_n p_n)}{(m_n - m^{\min}) + (m^{\max} - m_n) \exp(-\alpha_n \nu_n p_n)} q \quad \text{for } p_n > 0, \quad (40)$$

where

$$\alpha_n = \frac{m^{\max} - m^{\min}}{(m^{\max} - m_n)(m_n - m^{\min})}. \quad (41)$$

The details of the derivation of equations 39 and 40 can be found in Habashy and Abubakar (2004).

The iteration process ends if (1) the misfit  $\phi^d(\mathbf{m}_n)$  is within a prescribed tolerance factor, (2) the difference between the misfit at two successive iterates  $n$  is within a prescribed tolerance factor, (3) the difference between the model parameters  $\mathbf{m}$  at two successive iterates  $n$  is within a prescribed tolerance factor, or (4) the total number of iterations exceeds a prescribed maximum.

## NUMERICAL EXAMPLES

### Crosswell configuration

In this subsection, we apply our method to invert the data of crosswell EM measurements (Torres-Verdin and Habashy, 1994; Spies and Habashy, 1995; Wilt et al., 1995; Wilt and Alumbaugh, 1998; Abubakar and van den Berg, 2000). As a test example, we use the conductivity model shown in Figure 2. The color bars in the figures throughout this manuscript are given in  $\log(\sigma)$ .

In this test example, we have two blocky objects with conductivity 1 S/m (red object) and 0.1 S/m (blue object) embedded in a homogeneous medium with conductivity 0.5 S/m. These blocks are

25 m in the  $x$ -direction and 30 m in the  $z$ -direction. The data are collected using 33 transmitters and 33 receivers. The transmitters are vertical magnetic dipoles, and the measured data are the vertical components of the magnetic fields. The transmitter well is located at,  $x = -40$  m and the receiver well is located at  $x = 40$  m. The transmitters and receivers are distributed uniformly from  $z = -80$  m up to  $z = 80$  m. The frequency of operation is 500 Hz.

The synthetic data are generated by solving the forward problem using a 2.5D integral equation approach as described in Abubakar et al. (2006). After generating the synthetic data, we corrupt the data with random white noise that corre-

sponds to 2% of the maximum amplitude of all data points (at each frequency) according to the following formula:

$$d_{i,j,k}^{\text{obs,noise}} = d_{i,j,k}^{\text{obs}} + \frac{\max \nabla_{i,j} |d_{i,j,k}^{\text{obs}}|}{\sqrt{2}} \beta (\text{ran}_1 + i \text{ran}_2), \quad (42)$$

where  $\beta = 0.02$  is the noise level and  $\text{ran}_1$  and  $\text{ran}_2$  are two random number generators varying from  $-1$  to  $+1$ .

The inversion domain is from  $x = -60$  to  $60$  m and  $z = -80$  to  $80$  m and is discretized into grid cells measuring  $2.5 \times 2.5$  m; hence, the total number of unknown model parameters is 3072. The initial model used in the inversion is a homogeneous medium with conductivity  $0.5$  S/m. First, we run our inversion algorithm using the  $L_2$ -norm regularizer in equations 16 and 17. Using this regularization term, the scheme takes nine iterations to converge. At the end of the iteration, the data misfit cost function in equation 14 reduces to 1.56%. The inversion result is shown in Figure 2b. The image obtained in this case has the appearance of a spatially smoothed version of the true model in Figure 2a.

Next, we rerun our inversion code; however, we now use the weighted  $L_2$ -norm regularization factor in equations 16 and 18. The inversion results after eight iterations are shown in Figure 2c. By using the weighted  $L_2$ -norm regularizer, we obtain significant improvement in reconstructing the geometry of both blocky objects. After eight iterations, the data misfit cost function in equation 14 reduces to 1.44%. We also note the value of the conductivity of the resistive object (blue object) is underestimated. This is a typical drawback of an induction measurement, which is more sensitive to a conductive object than to a resistive one. Finally, we note that one iteration of the inversion scheme takes only 180 s on a PC with a Pentium IV 3.0-GHz processor.

Next, we present an inversion result of a data set collected in Lost Hills, California, (Wilt et al., 2005). The low recovery factors and flow rates made the operator in these oil wells experiment with waterflooding strategies, including tight well spacings and various injection strategies. These data sets were used to monitor reservoir changes at the pilot from 2001 to 2004. As Wilt et al. (2005, their Figure 1) show, four fiberglass-cased observation wells are available to measure the resistivity changes in the area. Since 2001, the crosswell data have been collected using all six possible well pairs. Next to these crosswell data, the individual induction resistivity logs were also measured. The reservoir consists of a roughly flat-lying sequence of alternating higher-resistivity layers ( $3\text{--}6$  ohm-m) associated with oil-bearing diatomites and silts with higher oil saturations and lower-resistivity ( $1\text{--}3$  ohm-m) intervening shales.

Here, we will show only the inversion results obtained using one of the well pairs, i.e., OB11-OB12 (see Figure 1 in Wilt et al., 2005). The data set was gathered using 55 transmitters located at  $x = 0$  and  $z = 341.17$  to  $588$  m as well as 76 receivers at  $x = 66.7$  to  $70$  m and  $z = 347.51$  to  $504$  m. Note that the receiver well was not entirely vertical; it was slightly deviated. Hence, the measured data are not entirely the vertical component of the magnetic field vector. This effect is taken into account in our forward simulator. The frequency of operation of the transmitters is 449.2 Hz.

In the inversion, we selected a domain measuring  $110 \times 110$  m. This inversion domain is discretized into  $22 \times 77$  grid cells. Hence, the size of the inversion cell is  $5 \times 5$  m. Because we did not have any crosswell measurement before the water injection experiment, we used as a starting model a resistivity distribution made from a number of induction single-well logs collected before the water injection

experiment (Figure 3a). The inverted conductivity model using the  $L_2$ -norm regularization function after seven iterations is shown in Figure 3b.

In Figure 3c, we plot also the normalized conductivity difference between Figure 3a and b according to the following formula:

$$\frac{\sigma_n(x,z) - \sigma_0(x,z)}{\sigma_0(x,z)} \times 100\%, \quad (43)$$

where  $\sigma_0$  and  $\sigma_n$  are the initial conductivity model and the one obtained after  $n$  iterations. The resistivity of the layer located between  $z = 500$  m and  $z = 530$  m decreases about 20%–30% because of the water injection. We also observe an increase in resistivity in some of the regions. The computational time of the inversion is about 140 s per iteration.

The inverted conductivity model and the changes using the weighted  $L_2$ -norm regularization function after 30 iterations are shown in Figure 4b and c. In the image obtained using the inversion algorithm with the weighted  $L_2$ -norm regularization, the resistivity decrease because of water injection is more pronounced than the one obtained using the  $L_2$ -norm regularization function. For more discussion on the Lost Hill data, see Wilt et al. (2005).

## Surface configuration

In this subsection, we apply our inversion approach to CSEM measurements (see Eidesmo et al., 2002; Ellingsrud et al., 2002; Tompkins, 2004; Johansen et al., 2005; Constable and Srnka, 2007).

The forward algorithm has been compared extensively to 2D model results generated by 3D codes. Here, we show only computations generated by our 2.5D forward algorithm compared to results from Zaslavsky et al. (2006). The test model consists of a reservoir region measuring  $8000 \times 100$  m (Figure 5). The hydrocarbon region has a conductivity of  $0.05$  S/m and is located at a depth of about 2 km from the sea surface. The water layer with conductivity of  $3$  S/m is between  $z = 0$  to  $1$  km. Above the water layer, we have an air layer from  $z = 0$  to  $-\infty$ . The conductivity of the seafloor is  $1$  S/m.

We show only a comparison of the horizontal component of the inline electric field (the transmitter is an electric dipole along the

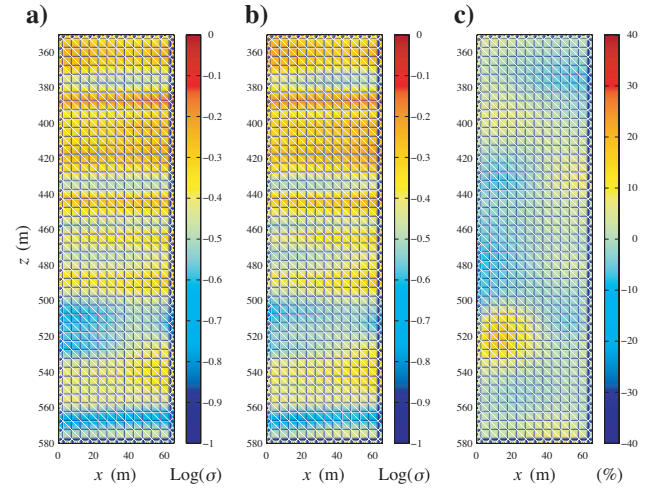


Figure 3. (a) The initial conductivity model; (b) the inverted conductivity model using the  $L_2$ -norm regularization; (c) the changes in the conductivity model of the Lost Hill data pair OB11-OB12.

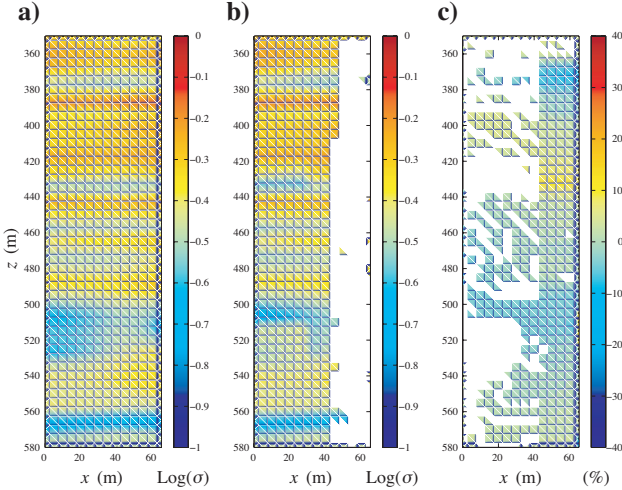


Figure 4. (a) The initial conductivity model; (b) the inverted conductivity model using the weighted  $L_2$ -norm regularization; (c) the changes in the conductivity model of the Lost Hill data pair OB11–OB12.

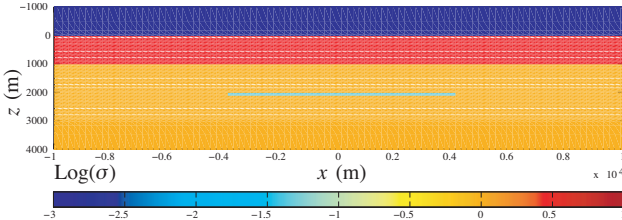


Figure 5. The synthetic CSEM test model for testing the forward and inversion method. The model consists of an 8-km-wide, 100-m-thick reservoir located at 1 km depth from the seafloor in a three-layered background medium consisting of air, water, and the seafloor.

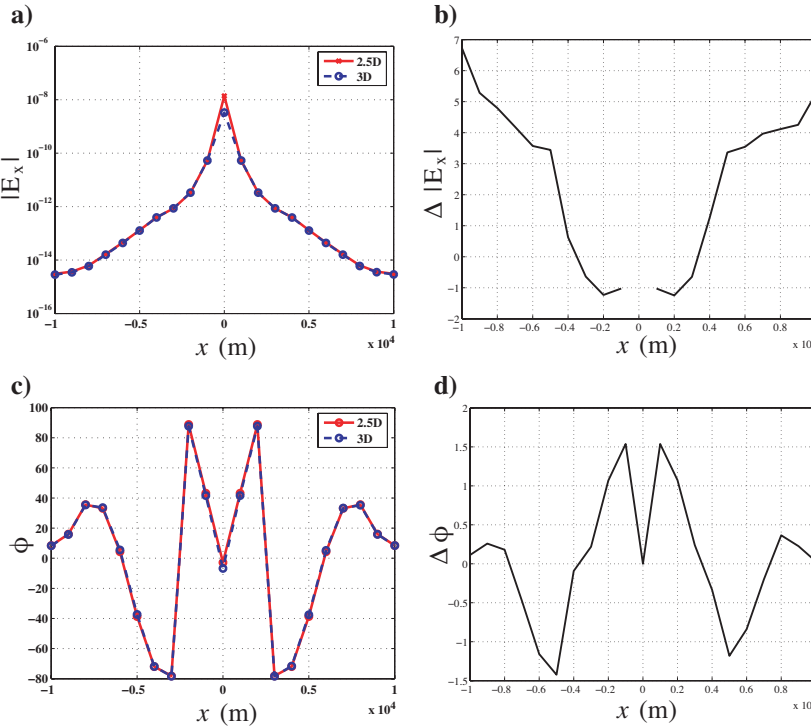


Figure 6. The inline electric-field comparison of the model in Figure 5 using the 3D and the 2.5D forward codes. (a) Amplitude of  $E_x$ . (b) Relative amplitude difference in percent. (c) Phase of  $E_x$ . (d) Absolute phase difference.

$x$ -direction and the measured electric field is along the  $x$ -direction). The transmitter is located at  $x = 0$  m and  $z = 0.95$  km, and its frequency of operation is 0.25 Hz. The receivers are located at depth  $z = 1$  km. A grid of 246 cells in the  $x$ -direction and 166 cells in the  $z$ -direction was used in the 2.5D code. The comparison is shown in Figure 6.

Figure 6a shows the amplitude of  $E_x$ , while Figure 6c shows the phase of  $E_x$ . Figure 6b and d gives the difference between two forward code responses. The maximum difference is about 6.5% in amplitude and 1.5° in phase (excluding the receiver at  $x = 0$  m). This agreement provides confidence that both solutions are fairly accurate. We observe a minor disagreement near the transmitter. This is probably caused by the singularity of the field close to the transmitter. The 3D code of Zaslavsky et al. (2006) does not have this limitation because it uses the scattered field formulation.

The computation time for the 2.5D algorithm was approximately five minutes on a PC with a 3.04-GHz processor. When we deal with more than one transmitter at the same frequency, the overhead computational time of the 2.5D forward algorithm is minimal because the code uses a direct solver. The code has been tested also for real and synthetic bathymetry profiles (see Zaslavsky et al., 2006).

To demonstrate the performance of the inversion algorithm, we again use the model shown in Figure 5. The data were generated for 21 seafloor receivers spaced at 1-km intervals, using 41 transmitters spaced at 0.5-km intervals located at depth  $z = 950$  m. The synthetic data set was generated using the 3D finite-difference code of Zaslavsky et al. (2006). After generating the synthetic data, 2% random white noise was added according to equation 42.

The inversion domain from  $x = -10$  to 10 km and from  $z = 1$  to 3 km is discretized into  $100 \times 60$  cells. The inversion results after 21 iterations using the  $L_2$ -norm regularization factor is shown in Figure

7a. After convergence, the normalized data misfit is reduced from 25.96% to 1.13%. The computational time was approximately six minutes per iteration on a PC with a 3.04-GHz Pentium processor. The inversion results using the weighted  $L_2$ -norm regularization factor are given in Figure 7b. Using this weighted  $L_2$ -norm regularization factor, after 30 iterations the normalized data misfit was reduced to 0.61%. By using this weighted  $L_2$ -norm regularization, we were able to obtain a better estimate of the width of the reservoir. However, the thickness of the reservoir was overestimated.

Next, we applied our inversion method to a field data set. The data were acquired over a portion of the Troll field in Norway using 23 electric dipole transmitters over a 13-km line at a depth of about  $z = 300$  m. Forty-five receiver units were laid out in a line over 24 km and located at a depth of about  $z = 320$  m. The electric dipole transmitter is nominally aligned with the survey line and ocean currents, producing some variation in the orientation of the transmitter along the line. In preprocessing, the time series is averaged to produce in-phase and out-of-phase electric fields. The transmitter fundamental is 0.25 Hz. There is sufficient power to extract the third and fifth harmonics so that three frequencies (0.25, 0.75, and 1.25 Hz) are acquired.

In the inversion, we selected a domain from  $x = -7$  to 19 km and  $z = 0.4$  to 3.5 km. This inversion domain was discretized into  $260 \times 62$  grid cells, making the size of a grid cell  $100 \times 50$  m. The initial model used in the inversion is shown in Figure 8. The model consists of an air layer, a water layer, and a seafloor layer. The conductivity of

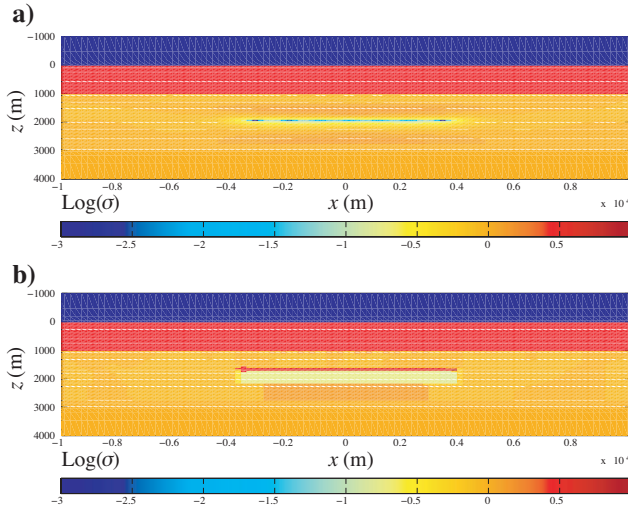


Figure 7. The inverted conductivity of the synthetic CSEM test example using (a) the  $L_2$ -norm regularization factor and (b) the weighted  $L_2$ -norm regularization factor.

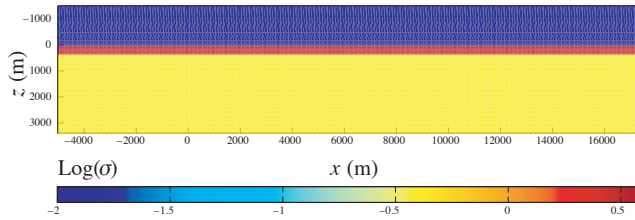


Figure 8. The initial model used to invert the Troll field data.

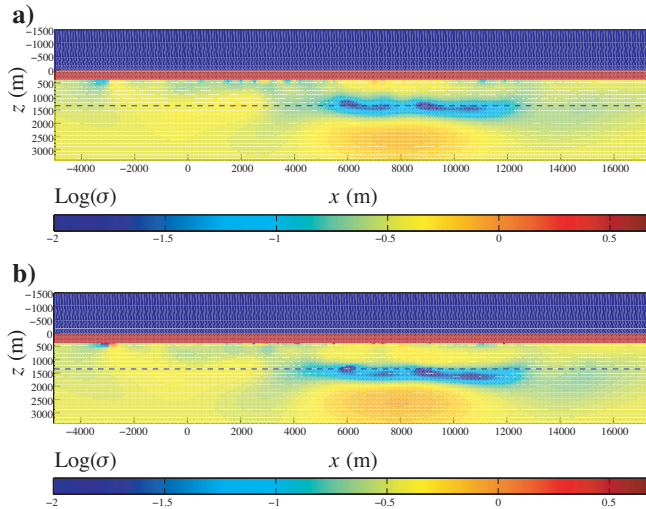


Figure 9. The inverted Troll field data at operating frequencies of 0.25 and 0.75 Hz using (a) the  $L_2$ -norm regularization function and (b) the weighted  $L_s$ -norm regularization function. The dashed line denotes the approximate reservoir depth derived from a seismic migration approach.

the water layer varies from 3.3 to 4 S/m, and the conductivity of the seafloor is 0.4 S/m. The inversion results of the data at 0.25 and 0.75 Hz after five iterations using the  $L_2$ -norm regularization function are shown in the Figure 9a. The depth of the reservoir estimated from seismic work is denoted by a dashed line. We observe the depth of the reservoir is estimated accurately. The inversion results after seven iterations using the weighted  $L_2$ -norm regularization function are shown in Figure 9b. The reservoir in the inversion results using the weighted  $L_2$ -norm regularization is nearly fully connected in the  $x$ -direction. The computational time of one iteration of this multifrequency scheme is approximately 23 minutes on a PC with a Pentium IV3.04-GHz processor.

## CONCLUSIONS

We have presented fast and rigorous forward and inversion algorithms for deep EM applications that include crosswell EM and controlled-source EM measurements.

The forward algorithm is based on a finite-difference approach in which the multifrontal LU decomposition algorithm simulates the multisource experiments. For problems with  $N$  finite-difference nodes, the multifrontal LU method takes  $O(N^{1.5})$  operations for matrix factorization and  $O(N \log N)$  for any additional source. The use of this direct solver is made possible by the optimal grid technique and a diagonal anisotropic material averaging formula.

The inversion algorithm uses a regularized Gauss-Newton minimization approach using the multiplicative cost function. By using this multiplicative cost function, we do not need to determine the so-called regularization parameter in the optimization process; hence, the algorithm is fully automated. The robustness of this approach is shown in the case study of crosswell and surface (CSEM) configuration. The algorithm is equipped by two regularization penalty functions, so it can produce either a smooth or a sharp conductivity distribution. To increase the robustness of the algorithm, we also used a line-search approach and a constrained minimization in the optimization process. Our synthetic and field data sets showed excellent speeds and accuracies of the developed methods.

These algorithms also can be used for the single-well measurement such as triaxial induction and surface-to-borehole EM measurements.

## ACKNOWLEDGMENTS

The authors thank Statoil and Electromagnetic Geoservices (EMGS) for access to the Troll field data and the Troll partners for permission to publish the results. They also thank Ping Zhang and Guozhong Gao of Schlumberger EMI for help in preparing the field data to test the inversion methods presented in this paper, Wenyi Hu from Schlumberger-Doll Research for his help in implementing the frequency weighting scheme, and Jianguo Liu from Schlumberger-Doll Research for his help in calibrating the field data. We also thank Mike Wilt from Schlumberger EMI for many useful discussions on crosswell EM measurements. Finally, the authors thank Mike Zaslavsky from Schlumberger-Doll Research for his help on benchmarking the forward algorithm.

## APPENDIX A ADJOINT SOLUTIONS

In this appendix, we derive the adjoint solutions needed to calculate the Jacobian matrix in equation 27.

### Magnetic dipole source

We cast the equation governing the electric field vector  $\mathbf{E}_K^s(\mathbf{r}, \mathbf{r}_s)$  at any point in space  $\mathbf{r}$  because of a magnetic current source  $\mathbf{K}_s(\mathbf{r}_s)$  located at  $\mathbf{r}_s$ , as follows:

$$\begin{aligned} \nabla \times \nabla \times \mathbf{E}_K^s(\mathbf{r}, \mathbf{r}_s) - i\omega\mu\sigma(\mathbf{r})\mathbf{E}_K^s(\mathbf{r}, \mathbf{r}_s) \\ = -\nabla \times \mathbf{K}_s(\mathbf{r}_s). \end{aligned} \quad (\text{A-1})$$

Denoting  $\tilde{\mathbf{E}}_K^s$  as the electric field vector resulting from a conductivity change of  $\sigma(\mathbf{r}) + \delta\sigma(\mathbf{r})$ , we have

$$\begin{aligned} \nabla \times \nabla \times \tilde{\mathbf{E}}_K^s(\mathbf{r}, \mathbf{r}_s) - i\omega\mu\{\sigma(\mathbf{r}) + \delta\sigma(\mathbf{r})\}\tilde{\mathbf{E}}_K^s(\mathbf{r}, \mathbf{r}_s) \\ = -\nabla \times \mathbf{K}_s(\mathbf{r}_s). \end{aligned} \quad (\text{A-2})$$

Defining the quantity

$$\delta\mathbf{E}_K^s(\mathbf{r}, \mathbf{r}_s) = \tilde{\mathbf{E}}_K^s(\mathbf{r}, \mathbf{r}_s) - \mathbf{E}_K^s(\mathbf{r}, \mathbf{r}_s), \quad (\text{A-3})$$

substituting equation A-3 into equation A-2, and using equation A-1, we obtain the following equation governing  $\delta\mathbf{E}_K^s(\mathbf{r}, \mathbf{r}_s)$ :

$$\begin{aligned} \nabla \times \nabla \times \delta\mathbf{E}_K^s(\mathbf{r}, \mathbf{r}_s) - i\omega\mu\sigma(\mathbf{r})\delta\mathbf{E}_K^s(\mathbf{r}, \mathbf{r}_s) \\ = i\omega\mu\delta\sigma(\mathbf{r})\tilde{\mathbf{E}}_K^s(\mathbf{r}, \mathbf{r}_s). \end{aligned} \quad (\text{A-4})$$

Defining the electric dyadic Green function caused by an electric source by

$$\begin{aligned} \nabla \times \nabla \times \mathcal{G}^{\text{EJ}}(\mathbf{r}, \mathbf{r}') - i\omega\mu\sigma(\mathbf{r})\mathcal{G}^{\text{EJ}}(\mathbf{r}, \mathbf{r}') \\ = i\omega\mu\mathcal{I}\delta(\mathbf{r} - \mathbf{r}'), \end{aligned} \quad (\text{A-5})$$

we obtain the integral equation governing  $\delta\mathbf{E}_K^s(\mathbf{r}, \mathbf{r}_s)$ :

$$\delta\mathbf{E}_K^s(\mathbf{r}, \mathbf{r}_s) = \int_{\tau_s} d\mathbf{r}' \delta\sigma(\mathbf{r}') \mathcal{G}^{\text{EJ}}(\mathbf{r}, \mathbf{r}') \cdot \tilde{\mathbf{E}}_K^s(\mathbf{r}', \mathbf{r}_s), \quad (\text{A-6})$$

where  $\tau_s$  is the support of  $\delta\sigma(\mathbf{r})$ .

### Electric dipole receiver

Because the generation of the dyadic Green function  $\mathcal{G}^{\text{EJ}}(\mathbf{r}, \mathbf{r}')$  for  $\mathbf{r} = \mathbf{r}_R$  (the receiver positions) and  $\mathbf{r}'$  (the computational domain) is expensive, we use the following reciprocity relation:

$$\mathcal{G}^{\text{EJ}}(\mathbf{r}, \mathbf{r}') = [\mathcal{G}^{\text{EJ}}(\mathbf{r}', \mathbf{r})]^t. \quad (\text{A-7})$$

Hence, we obtain

$$\delta\mathbf{E}_K^s(\mathbf{r}, \mathbf{r}_s) = \int_{\tau_s} d\mathbf{r}' \delta\sigma(\mathbf{r}') [\mathcal{G}^{\text{EJ}}(\mathbf{r}', \mathbf{r})]^t \cdot \tilde{\mathbf{E}}_K^s(\mathbf{r}', \mathbf{r}_s) \quad (\text{A-8})$$

$$= \int_{\tau_s} d\mathbf{r}' \delta\sigma(\mathbf{r}') \tilde{\mathbf{E}}_K^s(\mathbf{r}', \mathbf{r}_s) \cdot \mathcal{G}^{\text{EJ}}(\mathbf{r}', \mathbf{r}) \quad (\text{A-9})$$

In the limiting case of  $\delta\sigma \rightarrow 0$ , we arrive at

$$\delta\mathbf{E}_K^s(\mathbf{r}, \mathbf{r}_s) \approx \int_{\tau_s} d\mathbf{r}' \delta\sigma(\mathbf{r}') \mathbf{E}_K^s(\mathbf{r}', \mathbf{r}_s) \cdot \mathcal{G}^{\text{EJ}}(\mathbf{r}', \mathbf{r}). \quad (\text{A-10})$$

The electric field as sensed by a receiver located at  $\mathbf{r}_R$  and oriented along a particular direction is given by

$$\delta E_R(\mathbf{r}_R, \mathbf{r}_s) = \int_{\tau_s} d\mathbf{r}' \delta\sigma(\mathbf{r}') \mathbf{E}_K^s(\mathbf{r}', \mathbf{r}_s) \cdot \mathbf{E}_J^R(\mathbf{r}', \mathbf{r}_R), \quad (\text{A-11})$$

where  $\mathbf{E}_J^R(\mathbf{r}, \mathbf{r}_R)$  is the electric field at any point in space  $\mathbf{r}$  caused by an electric current source located at receiver location  $\mathbf{r}_R$  and oriented along the same direction as the receiver. This electric field satisfies the equation

$$\nabla \times \nabla \times \mathbf{E}_J^R(\mathbf{r}, \mathbf{r}_R) - i\omega\mu\sigma(\mathbf{r})\mathbf{E}_J^R(\mathbf{r}, \mathbf{r}_R) = i\omega\mu\mathbf{J}_R(\mathbf{r}_R). \quad (\text{A-12})$$

Because, within the support  $\tau_s$  of the conductivity anomaly, the conductivity distribution is assumed to be a constant, we finally arrive at

$$\frac{\delta E_R}{\delta\sigma_{\tau_s}}(\mathbf{r}_R, \mathbf{r}_s) = \int_{\tau_s} d\mathbf{r}' \mathbf{E}_K^s(\mathbf{r}', \mathbf{r}_s) \cdot \mathbf{E}_J^R(\mathbf{r}', \mathbf{r}_R). \quad (\text{A-13})$$

### Magnetic dipole receiver

The corresponding change in the magnetic field vector is given by

$$\begin{aligned} \delta\mathbf{H}_K^s(\mathbf{r}, \mathbf{r}_s) &= \frac{1}{i\omega\mu} \nabla \times \delta\mathbf{E}_K^s(\mathbf{r}, \mathbf{r}_s) \\ &= \int_{\tau_s} d\mathbf{r}' \delta\sigma(\mathbf{r}') \mathcal{G}^{\text{HJ}}(\mathbf{r}, \mathbf{r}') \cdot \tilde{\mathbf{E}}_K^s(\mathbf{r}', \mathbf{r}_s), \end{aligned} \quad (\text{A-14})$$

where

$$\mathcal{G}^{\text{HJ}}(\mathbf{r}, \mathbf{r}') = \frac{1}{i\omega\mu} \nabla \times \mathcal{G}^{\text{EJ}}(\mathbf{r}, \mathbf{r}'). \quad (\text{A-15})$$

According to reciprocity,

$$\mathcal{G}^{\text{HJ}}(\mathbf{r}, \mathbf{r}') = -[\mathcal{G}^{\text{EK}}(\mathbf{r}', \mathbf{r})]^t. \quad (\text{A-16})$$

Hence, we obtain

$$\delta\mathbf{H}_K^s(\mathbf{r}, \mathbf{r}_s) = - \int_{\tau_s} d\mathbf{r}' \delta\sigma(\mathbf{r}') [\mathcal{G}^{\text{EK}}(\mathbf{r}', \mathbf{r})]^t \cdot \tilde{\mathbf{E}}_K^s(\mathbf{r}', \mathbf{r}_s) \quad (\text{A-17})$$

$$= - \int_{\tau_s} d\mathbf{r}' \delta\sigma(\mathbf{r}') \tilde{\mathbf{E}}_K^s(\mathbf{r}', \mathbf{r}_s) \cdot \mathcal{G}^{EK}(\mathbf{r}', \mathbf{r}). \quad (\text{A-18})$$

In the limiting case of  $\delta\sigma \rightarrow 0$ , we arrive at

$$\delta\mathbf{H}_K^s(\mathbf{r}, \mathbf{r}_s) \approx - \int_{\tau_s} d\mathbf{r}' \delta\sigma(\mathbf{r}') \mathbf{E}_K^s(\mathbf{r}', \mathbf{r}_s) \cdot \mathcal{G}^{EK}(\mathbf{r}', \mathbf{r}). \quad (\text{A-19})$$

The magnetic field as sensed by a receiver located at  $\mathbf{r}_R$  and oriented along a particular direction is given by

$$\delta H_R(\mathbf{r}_R, \mathbf{r}_s) = - \int_{\tau_s} d\mathbf{r}' \delta\sigma(\mathbf{r}') \mathbf{E}_K^s(\mathbf{r}', \mathbf{r}_s) \cdot \mathbf{E}_K^R(\mathbf{r}', \mathbf{r}_R), \quad (\text{A-20})$$

where  $\mathbf{E}_K^R(\mathbf{r}, \mathbf{r}_R)$  is the electric field at any point in space  $\mathbf{r}$  because of a magnetic current source located at the receiver location  $\mathbf{r}_R$  and oriented along the same direction as the receiver. This electric field vector satisfies the equation

$$\begin{aligned} \nabla \times \nabla \times \mathbf{E}_K^R(\mathbf{r}, \mathbf{r}_R) - i\omega\mu\sigma(\mathbf{r}) \mathbf{E}_K^R(\mathbf{r}, \mathbf{r}_R) \\ = -\nabla \times \mathbf{K}_R(\mathbf{r}_R). \end{aligned} \quad (\text{A-21})$$

Within the support  $\tau_s$  of the conductivity anomaly, the conductivity distribution is assumed to be a constant, so we finally have

$$\frac{\delta H_R}{\delta\sigma_{\tau_s}}(\mathbf{r}_R, \mathbf{r}_s) = - \int_{\tau_s} d\mathbf{r}' \mathbf{E}_K^R(\mathbf{r}', \mathbf{r}_R) \cdot \mathbf{E}_K^s(\mathbf{r}', \mathbf{r}_s). \quad (\text{A-22})$$

### Electric dipole source

In the case of an electric dipole source, we cast the equation governing the electric field  $\mathbf{E}_J^s(\mathbf{r}, \mathbf{r}_s)$  at any point in space  $\mathbf{r}$  resulting from an electric current source  $\mathbf{J}_s(\mathbf{r}_s)$  located at  $\mathbf{r}_s$  as

$$\nabla \times \nabla \times \mathbf{E}_J^s(\mathbf{r}, \mathbf{r}_s) - i\omega\mu\sigma(\mathbf{r}) \mathbf{E}_J^s(\mathbf{r}, \mathbf{r}_s) = i\omega\mu\mathbf{J}_s(\mathbf{r}_s). \quad (\text{A-23})$$

Denoting  $\tilde{\mathbf{E}}_J^s$  as the electric field resulting from a conductivity change of  $\sigma(\mathbf{r}) + \delta\sigma(\mathbf{r})$ , we have

$$\begin{aligned} \nabla \times \nabla \times \tilde{\mathbf{E}}_J^s(\mathbf{r}, \mathbf{r}_s) - i\omega\mu[\sigma(\mathbf{r}) + \delta\sigma(\mathbf{r})] \tilde{\mathbf{E}}_J^s(\mathbf{r}, \mathbf{r}_s) \\ = i\omega\mu\mathbf{J}_s(\mathbf{r}_s). \end{aligned} \quad (\text{A-24})$$

Defining

$$\delta\mathbf{E}_J^s(\mathbf{r}, \mathbf{r}_s) = \tilde{\mathbf{E}}_J^s(\mathbf{r}, \mathbf{r}_s) - \mathbf{E}_J^s(\mathbf{r}, \mathbf{r}_s), \quad (\text{A-25})$$

substituting equation A-25 into equation A-24, and using equation A-23, we obtain the equation governing  $\delta\mathbf{E}_J^s(\mathbf{r}, \mathbf{r}_s)$ :

$$\begin{aligned} \nabla \times \nabla \times \delta\mathbf{E}_J^s(\mathbf{r}, \mathbf{r}_s) - i\omega\mu\sigma(\mathbf{r}) \delta\mathbf{E}_J^s(\mathbf{r}, \mathbf{r}_s) \\ = i\omega\mu\delta\sigma(\mathbf{r}) \tilde{\mathbf{E}}_J^s(\mathbf{r}, \mathbf{r}_s). \end{aligned} \quad (\text{A-26})$$

Using the definition of the electric dyadic Green function resulting

from an electric source in equation A-5, we obtain the following integral equation governing  $\delta\mathbf{E}_J^s(\mathbf{r}, \mathbf{r}_s)$ :

$$\delta\mathbf{E}_J^s(\mathbf{r}, \mathbf{r}_s) = \int_{\tau_s} d\mathbf{r}' \delta\sigma(\mathbf{r}') \mathcal{G}^{EJ}(\mathbf{r}, \mathbf{r}') \cdot \tilde{\mathbf{E}}_J^s(\mathbf{r}', \mathbf{r}_s), \quad (\text{A-27})$$

where  $\tau_s$  is the support of  $\delta\sigma(\mathbf{r})$ .

### Electric dipole receiver

To reduce the computational expenses, we use the following reciprocity relation:

$$\mathcal{G}^{EJ}(\mathbf{r}, \mathbf{r}') = [\mathcal{G}^{EJ}(\mathbf{r}', \mathbf{r})]^t. \quad (\text{A-28})$$

Hence, we obtain

$$\begin{aligned} \delta\mathbf{E}_J^s(\mathbf{r}, \mathbf{r}_s) &= \int_{\tau_s} d\mathbf{r}' \delta\sigma(\mathbf{r}') [\mathcal{G}^{EJ}(\mathbf{r}', \mathbf{r})]^t \cdot \tilde{\mathbf{E}}_J^s(\mathbf{r}', \mathbf{r}_s) \\ &= \int_{\tau_s} d\mathbf{r}' \delta\sigma(\mathbf{r}') \tilde{\mathbf{E}}_J^s(\mathbf{r}', \mathbf{r}_s) \cdot \mathcal{G}^{EJ}(\mathbf{r}', \mathbf{r}). \end{aligned} \quad (\text{A-29})$$

In the limiting case of  $\delta\sigma \rightarrow 0$ , we arrive at

$$\delta\mathbf{E}_J^s(\mathbf{r}, \mathbf{r}_s) \approx \int_{\tau_s} d\mathbf{r}' \delta\sigma(\mathbf{r}') \mathbf{E}_J^s(\mathbf{r}', \mathbf{r}_s) \cdot \mathcal{G}^{EJ}(\mathbf{r}', \mathbf{r}). \quad (\text{A-31})$$

The electric field as sensed by a receiver located at  $\mathbf{r}_R$  and oriented along a particular direction is given by

$$\delta E_R(\mathbf{r}_R, \mathbf{r}_s) = \int_{\tau_s} d\mathbf{r}' \delta\sigma(\mathbf{r}') \mathbf{E}_J^s(\mathbf{r}', \mathbf{r}_s) \cdot \mathbf{E}_J^R(\mathbf{r}', \mathbf{r}_R), \quad (\text{A-32})$$

where  $\mathbf{E}_J^R(\mathbf{r}, \mathbf{r}_R)$  is the electric field at any point in space  $\mathbf{r}$  resulting from an electric current source located at  $\mathbf{r}_R$  and oriented along the same direction as the receiver. It is governed by

$$\nabla \times \nabla \times \mathbf{E}_J^R(\mathbf{r}, \mathbf{r}_R) - i\omega\mu\sigma(\mathbf{r}) \mathbf{E}_J^R(\mathbf{r}, \mathbf{r}_R) = i\omega\mu\mathbf{J}_R(\mathbf{r}_R). \quad (\text{A-33})$$

Within the support  $\tau_s$  of the conductivity anomaly, the conductivity distribution is assumed to be a constant, so we finally have

$$\frac{\delta E_R}{\delta\sigma_{\tau_s}}(\mathbf{r}_R, \mathbf{r}_s) = \int_{\tau_s} d\mathbf{r}' \mathbf{E}_J^s(\mathbf{r}', \mathbf{r}_s) \cdot \mathbf{E}_J^R(\mathbf{r}', \mathbf{r}_R). \quad (\text{A-34})$$

### Magnetic dipole receiver

The change in terms of the magnetic field is given by the following equation:

$$\delta\mathbf{H}_J^s(\mathbf{r}, \mathbf{r}_s) = \frac{1}{i\omega\mu} \nabla \times \delta\mathbf{E}_J^s(\mathbf{r}, \mathbf{r}_s)$$

$$= \int_{\tau_s} d\mathbf{r}' \delta\sigma(\mathbf{r}') \mathcal{G}^{HJ}(\mathbf{r}, \mathbf{r}') \cdot \tilde{\mathbf{E}}_J^s(\mathbf{r}', \mathbf{r}_s), \quad (\text{A-35})$$

where

$$\mathcal{G}^{HJ}(\mathbf{r}, \mathbf{r}_s) = \frac{1}{i\omega\mu} \nabla \times \mathcal{G}^{EJ}(\mathbf{r}, \mathbf{r}_s). \quad (\text{A-36})$$

Using the reciprocity relation in equation A-16, we obtain

$$\delta\mathbf{H}_J^s(\mathbf{r}, \mathbf{r}_s) = - \int_{\tau_s} d\mathbf{r}' \delta\sigma(\mathbf{r}') [\mathcal{G}^{EK}(\mathbf{r}', \mathbf{r})]^t \cdot \tilde{\mathbf{E}}_J^s(\mathbf{r}', \mathbf{r}_s) \quad (\text{A-37})$$

$$= - \int_{\tau_s} d\mathbf{r}' \delta\sigma(\mathbf{r}') \tilde{\mathbf{E}}_J^s(\mathbf{r}', \mathbf{r}_s) \cdot \mathcal{G}^{EK}(\mathbf{r}', \mathbf{r}). \quad (\text{A-38})$$

In the limiting case of  $\delta\sigma \rightarrow 0$ , we arrive at

$$\delta\mathbf{H}_J^s(\mathbf{r}, \mathbf{r}_s) \approx - \int_{\tau_s} d\mathbf{r}' \delta\sigma(\mathbf{r}') \mathbf{E}_J^s(\mathbf{r}', \mathbf{r}_s) \cdot \mathcal{G}^{EK}(\mathbf{r}', \mathbf{r}). \quad (\text{A-39})$$

The magnetic field as sensed by a receiver located at  $\mathbf{r}_R$  and oriented along a particular direction is given by

$$\delta H_R(\mathbf{r}_R, \mathbf{r}_s) = - \int_{\tau_s} d\mathbf{r}' \delta\sigma(\mathbf{r}') \mathbf{E}_J^s(\mathbf{r}', \mathbf{r}_s) \cdot \mathbf{E}_K^R(\mathbf{r}', \mathbf{r}_R), \quad (\text{A-40})$$

where  $\mathbf{E}_K^R(\mathbf{r}, \mathbf{r}_R)$  is the electric field at any point in space  $\mathbf{r}$  resulting from a magnetic-current source located at the receiver location  $\mathbf{r}_R$  and oriented along the same direction as the receiver. It is governed by equation A-21. Because within the support  $\tau_s$  of the conductivity anomaly the conductivity distribution is assumed to be a constant, we finally have

$$\frac{\delta H_R}{\delta\sigma_{\tau_s}}(\mathbf{r}_R, \mathbf{r}_s) = - \int_{\tau_s} d\mathbf{r}' \mathbf{E}_J^s(\mathbf{r}', \mathbf{r}_s) \cdot \mathbf{E}_K^R(\mathbf{r}', \mathbf{r}_R). \quad (\text{A-41})$$

## REFERENCES

- Abubakar, A., and P. M. van den Berg, 2000, Three-dimensional inverse scattering applied to cross-well induction sensors: *IEEE Transactions on Geoscience and Remote Sensing*, **38**, 1669–1681.
- Abubakar, A., P. M. van den Berg, and T. M. Habashy, 2006, An integral equation approach for 2.5 dimensional forward and inverse electromagnetic scattering: *Geophysical Journal International*, **165**, 744–762.
- Allers, A., A. Sezginer, and V. L. Druskin, 1994, Solution of 2.5-dimensional problems using the Lanczos decomposition: *Radio Science*, **29**, 955–963.
- Chan, T. F., and C. K. Wong, 1998, Total variation blind deconvolution: *IEEE Transactions on Image Processing*, **7**, 370–375.
- Charbonnier, P., L. Blanc-Féraud, G. Aubert, and M. Barlaud, 1996, Deterministic edge-preserving regularization in computed imaging: *IEEE Transactions on Image Processing*, **6**, 298–311.
- Constable, S., and L. J. Srnka, 2007, An introduction to marine controlled-source electromagnetic methods for hydrocarbon exploration: *Geophysics*, **72**, no. (5), WA3–WA12.
- Davis, T. A., 2007, Direct methods for sparse linear systems: Society for Industrial and Applied Mathematics.
- Davis, T. A., and I. S. Duff, 1997, An unsymmetric pattern multifrontal method for sparse LU factorization: *SIAM Journal on Matrix Analysis and Applications*, **18**, 140–158.
- Dennis, J. E., Jr., and R. B. Schnabel, 1983, Numerical methods for unconstrained optimization and nonlinear equations: Prentice Hall, Inc.
- Dobson, D. C., and F. Santosa, 1996, An image-enhancement technique for electrical impedance tomography: *Inverse Problems*, **10**, 317–334.
- Druskin, V. L., and L. A. Knizhnerman, 1994, Spectral approach to solving three-dimensional Maxwell's diffusion equations in the time and frequency domain: *Radio Science*, **29**, 937–953.
- Eidesmo, T., S. Ellingsrud, L. M. MacGregor, S. Constable, M. C. Sinha, S. Johansen, F. N. Kong, and H. Westerdahl, 2002, Sea bed logging (SBL), a new method for remote and direct identification of hydrocarbon filled layers in deepwater areas: *First Break*, **20**, 144–152.
- Ellingsrud, S., T. Eidesmo, and S. Johansen, 2002, Remote sensing of hydrocarbon layers by seabed logging (SBL): Results from a cruise offshore Angola: *The Leading Edge*, **21**, 972–982.
- Farquharson, C. G., and D. Oldenburg, 1998, Non-linear inversion using general measures of data misfit and model structure: *Geophysical Journal International*, **134**, 213–227.
- Golub, G. H., and C. F. van Loan, 1989, Matrix computations: The Johns Hopkins University Press.
- Gribenko, A., and M. Zhdanov, 2007, Rigorous 3D inversion of marine CSEM data based on the integral equation method: *Geophysics*, **72**, no. (2), WA73–WA83.
- Habashy, T. M., and A. Abubakar, 2004, A general framework for constraint minimization for the inversion of electromagnetic measurements: *Progress in Electromagnetic Research*, **46**, 265–312.
- , 2007, A generalized material averaging formulation for modelling of the electromagnetic fields: *Journal of Electromagnetic Waves and Applications*, **21**, 1145–1159.
- Hoversten, G. M., J. Chen, E. Gasperikova, and G. Newman, 2005, Integration of marine CSEM and seismic AVA data for reservoir parameter estimation: 75th Annual International Meeting, SEG, Expanded Abstracts, 579–582.
- Ingerman, D., V. L. Druskin, and L. Knizhnerman, 2000, Optimal finite difference grids and rational approximations of the square root, I: Elliptic problems: *Communications on Pure and Applied Mathematics*, **53**, 1039–1066.
- Johansen, S. E., H. E. F. Amundsen, T. Rosten, S. Ellingsrud, T. Eidesmo, and A. H. Bhuyian, 2005, Subsurface hydrocarbons detected by electromagnetic sounding: *First Break*, **23**, 31–36.
- Keller, J. B., 1964, A theorem on the conductivity of a composite medium: *Journal of Mathematical Physics*, **5**, 548–549.
- MacGregor, L. M., and M. C. Sinha, 2000, Use of marine controlled source electromagnetic sounding for sub-basalt exploration: *Geophysical Prospecting*, **48**, 1091–1106.
- Mackie, R. L., and T. R. Madden, 1993, Three-dimensional magnetotelluric inversion using conjugate gradients: *Geophysical Journal International*, **115**, 215–229.
- McGillivray, P. R., and D. W. Oldenburg, 1990, Methods for calculating Frechet derivatives and sensitivities for the non-linear inverse problem: *Geophysical Prospecting*, **38**, 499–524.
- Mittet, R., F. Maao, O. M. Aakervik, and S. Ellingsrud, 2005, A two-step approach to depth migration of low-frequency electromagnetic data: 75th Annual International Meeting, SEG, Expanded Abstracts, 522–525.
- Moskow, S., V. Druskin, T. M. Habashy, P. Lee, and S. Davydychava, 1999, A finite difference scheme for elliptic equations with rough coefficients using a Cartesian grid nonconforming to interfaces: *SIAM Journal of Numerical Analysis*, **36**, 442–464.
- Newman, G. A., and D. L. Alumbaugh, 1997, Three-dimensional massively parallel electromagnetic inversion: I — Theory: *Geophysical Journal International*, **128**, 345–354.
- Newman, G. A., and P. T. Boggs, 2004, Solution accelerators for large-scale three-dimensional electromagnetic inverse problems: *Inverse Problems*, **20**, S151–S170.
- Portniaguine, O., and M. S. Zhdanov, 1999, Focusing geophysical inversion images: *Geophysics*, **64**, 874–887.
- Rodi, W., and R. L. Mackie, 2001, Nonlinear conjugate gradients algorithm for 2D magnetotelluric inversion: *Geophysics*, **66**, 174–187.
- Rudin, L., S. Osher, and C. Fatemi, 1992, Nonlinear total variation based on noise removal algorithm: *Physica*, **30D**, 259–268.
- Spies, B. R., and T. M. Habashy, 1995, Sensitivity analysis of crosswell electromagnetics: *Geophysics*, **50**, 834–845.
- Tompkins, M. J., 2004, Marine controlled-source electromagnetic imaging for hydrocarbon exploration: *First Break*, **22**, 45–51.
- Torres-Verdín, C., and T. M. Habashy, 1994, Rapid 2.5-D forward modeling and inversion via a new nonlinear scattering approximation: *Radio Science*, **29**, 1051–1079.
- van den Berg, P. M., A. L. van Broekhoven, and A. Abubakar, 1999, Extend-

- ed contrast source inversion: Inverse Problems, **15**, 1325–1344.
- van den Berg, P. M., and A. Abubakar, 2001, Contrast source inversion method: State of art: Progress in Electromagnetics Research, **34**, 189–218.
- Vogel, C. R., and M. E. Oman, 1996, Iterative methods for total variation denoising: SIAM Journal on Scientific Computing, **17**, 227–238.
- Wilt, M. J., and D. L. Alumbaugh, 1998, Electromagnetic methods for development and production: State of the art: The Leading Edge, **17**, 450–548.
- Wilt, M. J., D. L. Alumbaugh, F. Morrison, A. Becker, K. H. Lee, and M. Deszcz-Pan, 1995, Crosswell electromagnetic tomography: System design considerations and field results: Geophysics, **60**, 871–885.
- Wilt, M. J., J. Little, P. Zhang, and J. Chen, 2005, Using crosswell EM to track waterflooding at the Lost Hill oil field: 75th Annual International Meeting, SEG, Expanded Abstracts, 1269–1272.
- Yee, K. S., 1966, Numerical solution of initial boundary value problems involving Maxwell's equations in isotropic media: IEEE Transactions on Antennas and Propagation, **14**, 302–307.
- Zaslavsky, M., S. Davydcheva, V. L. Druskin, L. Knizherman, A. Abubakar, and T. M. Habashy, 2006, Finite difference solution of the three-dimensional electromagnetic problem using divergence free preconditioners: 76th Annual International Meeting, SEG, Expanded Abstracts, session EM2.8.